Inorganic Chemistry

pubs.acs.org/IC

Article

Open Access

This article is licensed under CC-BY 4.0

Opposite Effects of Added $AsPh_3$ Reveal a Drastic Mechanistic Switch in Rh^I/Au^I Transmetalations via Rh−Au Bonded Intermediates

Marconi N. Peñas-Defrutos,* Camino Bartolomé, Max García-Melchor, and Pablo Espinet*

Cite This: *Inorg. Chem.* 2025, 64, 13729−13739

Read Online

ACCESS | Metrics & More | Article Recommendations | Supporting Information

ABSTRACT: In contrast with the previously reported decelerating effect of added L (L = $AsPh_3$) on the Rf/Pf exchange reaction between [Au(Pf)L] and *trans*-[Rh(Rf)(CO)L_2] (Pf = C_6F_5; Rf = $C_6F_3Cl_2$-3,5), the Rf/Cl exchange between [AuClL] and *trans*-[Rh(Rf)(CO)L_2] is accelerated by addition of an excess of L. By combining experimental data and microkinetic modeling, with DFT calculations, the unexpected existence of two cooperative Rf/Cl exchange mechanisms is demonstrated. The opposite kinetic effects of L addition, from negative in the Rf/Pf exchange process, opposing L dissociation in an octahedral rhodium intermediate, to positive in the Rf/Cl exchange, opening an L-catalyzed alternative pathway via tricoordinate gold intermediates, explain the Janus effect of $AsPh_3$. The three transmetalation pathways involve a metal redox-insertion step with accessible activation barrier, producing intermediates with Rh−Au bonds. Whereas our previously reported Rf/Pf exchange implied Rh(I) oxidation by Au(I), the Rf/Cl exchange mechanism involves Au(I) oxidation by Rh(I). Further support is provided by NBO studies, which reveal remarkable electronic donations from the oxidized metal in each case forging the M−M′ covalent interaction in the intermediates yielded by the redox-insertion step.

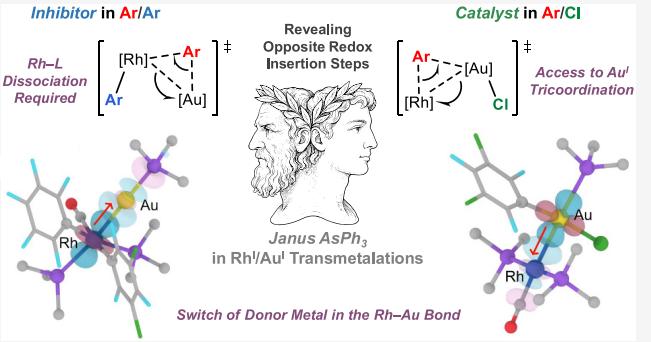

INTRODUCTION

A most common transmetalation in catalysis is R for X exchange (R = organic group on a main group element; X = halide on a transition metal). It usually occurs via μ-X μ-R double-bridged intermediates. For other transmetalations, such as R/R′ exchanges (responsible for undesired homocoupling products), different mechanisms have been reported. For instance, while for the $ClAu^I/PhSn^{IV}$ exchange, the classical double-bridged mechanism was reported, for the (vinyl)$Au^I/PhSn^{IV}$ transmetalation, an oxidative addition/reductive elimination (OA/RE) pathway, via an intermediate featuring an Au−Sn bond, was found.[1]

In the growing field of bimetallic catalysis, which deals with homogeneous processes where either two transition metals (TM),[2] or one TM and one group-11 element,[3] cooperate in a catalytic transformation (often a C−C coupling), the exchange mechanisms can follow diverse pathways. Examples are the Pd/Au cooperativity in gold cocatalyzed Stille coupling of bulky aryls,[4] or the now popular Pd−Cu catalyzed cross-coupling processes.[5] Better understanding of the transmetalation mechanisms operating in these processes may facilitate the design of more efficient systems.

The scarcity of mechanistic studies on Rh^I/Au^I transmetalations prompted us to investigate this promising catalytic dyad.[6,7] In this context, we have already reported the mechanism of aryl/aryl' scrambling between the Vaska-type complex *trans*-[Rh(Rf)(CO)$(AsPh_3)_2$] (**1**) (Rf = $C_6F_3Cl_2$-3,5) and [Au(Pf)$(AsPh_3)$] (Pf = C_6F_5), shown in eq 1.[8] The

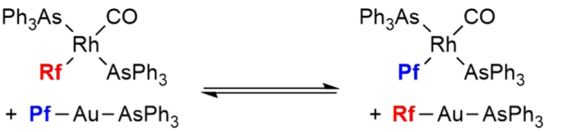

(1)

unconventional fractional and negative rate dependence of this aryl/aryl' exchange upon free $AsPh_3$ addition (Figure 1A) suggested a rather complex reaction mechanism. In fact, this exchange follows an OA/RE pathway via redox insertion of Rh into the Au−C bond), which indicates that Rh^I is formally oxidized by Au^I. Figure 1B depicts the computed transition state illustrating the insertion. This initial step leads to an intermediate with octahedral Rh, linear Au, and a Rh^{II}−Au^0

Received: March 8, 2025
Revised: June 12, 2025
Accepted: June 20, 2025
Published: June 26, 2025

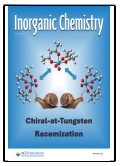

Downloaded via UNIVERSIDAD DE VALLADOLID on November 11, 2025 at 10:48:09 (UTC).
See https://pubs.acs.org/sharingguidelines for options on how to legitimately share published articles.

© 2025 The Authors. Published by American Chemical Society

https://doi.org/10.1021/acs.inorgchem.5c01081
Inorg. Chem. 2025, 64, 13729−13739

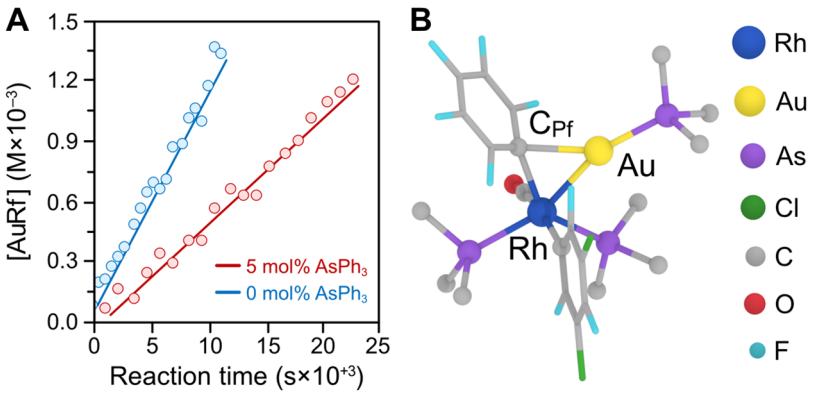

Figure 1. (A) Kinetic effect of added ligand on the transmetalation rate in eq 1. (B) DFT-calculated transition state for the Rh insertion into the Au−C_{Pf} bond. The Ph groups in the arsine are simplified to their C_{ipso} for clarity. Figure adapted with permission from ref 8. Copyright [2019][Wiley].

bond.[9] The M/M′ redox process looks quite reasonable considering the oxidizing power of Au(I). The retarding effect of added $AsPh_3$ is due to a rate determining isomerization step in the transmetalation pathway, which requires $AsPh_3$ dissociation from Rh in the octahedral intermediate resulting from the redox insertion.[8]

RESULTS AND DISCUSSION

Experimental Kinetic Studies. Herein we report the Rf/Cl transmetalation reaction between *trans*-[Rh(Rf)(CO)-$(AsPh_3)_2$] (**1**) and [AuCl$(AsPh_3)$] (**2**) yielding *trans*-[RhCl-$(CO)(AsPh_3)_2$] (**3**) + [Au(Rf)$(AsPh_3)$] (**4**) (eq 2).[10] The use

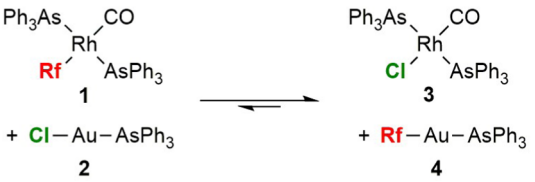

(2)

of Cl in the gold reagent, instead of Pf, seems to produce a dramatic mechanistic change hinted by the fact that the addition of $AsPh_3$ accelerates the process instead of retarding it.[8] More precisely, $AsPh_3$ has a catalytic effect on the Rf/Cl exchange. In CD_2Cl_2, the exchange equilibrium of (eq 2) is largely shifted to formation of **3** + **4**. It was monitored by ^{19}F NMR in both senses, using stoichiometric conditions (1:1 molar ratio) until steady concentrations of the species were reached (24 h at room temperature).[11] This afforded an equilibrium constant $K_{eq} = 7.0 \times 10^3$ ($\Delta G_0 = -5.2$ kcal mol^{-1}) corresponding to 99% conversion to **3** + **4** (Figure S1), revealing complex **1** as a thermodynamically efficient aryl transmetalating agent to gold(I). Neither other products nor reaction intermediates were detected. Experiments using 2:1 or 1:2 Au:Rh ratios doubled the reaction rate observed for the stoichiometric 1:1 reaction, confirming first order reaction kinetics in both reactants (Figure S2). Finally, as mentioned above, the addition of $AsPh_3$ resulted in a significant and unexpected increase of reaction rate, in striking contrast with the clear deceleration shown in the case of Rf/Pf exchange.[8]

Figure 2 plots the experimental points of the ^{19}F NMR monitoring of the exchanges with different additions of free $AsPh_3$ (CD_2Cl_2, 273 K). Least squares adjustment of the data for the reaction in the absence of added $AsPh_3$ (Figure 2, red dots) yielded an initial reaction rate $r_0 = 2.16 \times 10^{-7}$ mol L^{-1} s^{-1}, corresponding to a Gibbs activation energy $\Delta G_{273\,K}^{\ddagger} = 19.2$ kcal mol^{-1} (see kinetic section in the SI for details). The addition of only 10 mol % $AsPh_3$ relative to gold concentration accelerated the initial transmetalation rate by *ca.* 60% (deep blue dots), and a 4-fold rate increase was observed with 60 mol % of $AsPh_3$ (pink dots). Hence, the observed $AsPh_3$ dependence is not linear. Moreover, the transmetalation rate seems to level off at large overstoichiometric ligand concentrations and subsequent additions of $AsPh_3$ to the last sequence of points represented (500% mol of $AsPh_3$, light blue dots) hardly produce any significant rate change (see Table S2 for details).

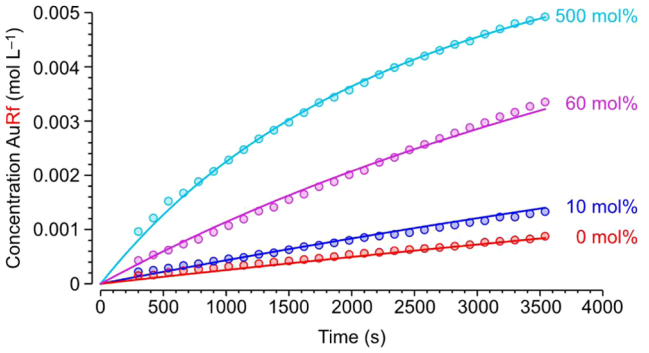

Figure 2. Concentration vs time data (circles) obtained by monitoring the formation of product [Au(Rf)$(AsPh_3)$] (**4**) by means of ^{19}F NMR in CD_2Cl_2 at 273 K with different percentages of added $AsPh_3$. Initial concentrations of the reactants: $[Rh]_0 = [Au]_0 = 1.0 \times 10^{-2}$ mol L^{-1}. Lines represent data adjusted with COPASI software.

The continuous lines in Figure 2 correspond to the overall adjustment of all the data, using COPASI software,[12] to the kinetic model shown in Scheme 1. The model consists of two

Scheme 1. Kinetic Model for COPASI Fitting of the $AsPh_3$ Catalytic Effect. L = $AsPh_3$. Ligands in the Rh Complex Omitted for Clarity

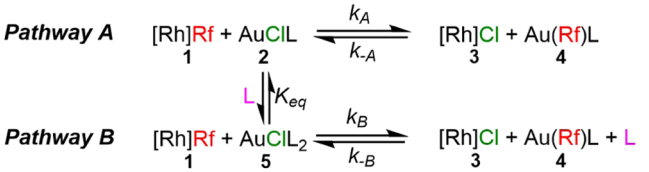

https://doi.org/10.1021/acs.inorgchem.5c01081
Inorg. Chem. 2025, 64, 13729−13739

competitive pathways (**A** and **B**) connected by an equilibrium of $AsPh_3$ coordination to **2**, forming the tricoordinate species $[AuCl(AsPh_3)_2]$ (**5**). The reaction without added $AsPh_3$ proceeds through pathway **A**, whereas in the presence of added $AsPh_3$ the two pathways sum up. **A** and **B** give the same end products, hence pathway **B** is an $AsPh_3$-catalyzed variation of pathway **A**.

This mechanistic proposal is based on a study reporting that expansion of the Au(I) linear coordination of $[AuX(AsPh_3)]$ complexes occurs upon $AsPh_3$ addition, giving rise to multiple coordination equilibria involving $[AuX(AsPh_3)_m]$ structures (X = halide; m = 1, 2, 3). These structures display progressive elongation of the Au−X bond upon successive coordinations of $AsPh_3$.[13] In our study, intermediate **5**, lacking ^{19}F, cannot be detected in the ^{19}F NMR monitoring but mass spectrometry confirmed the formation of $[AuCl(AsPh_3)_2]$ (**5**) in CH_2Cl_2 with substoichiometric amounts of $AsPh_3$, whereas $[AuCl(AsPh_3)_3]$, plausible to be formed at large excess of $AsPh_3$, was not detected. On the other hand, the ^{19}F NMR spectra detected only $[Au(Rf)(AsPh_3)]$ (**4**) but not $[Au(Rf)(AsPh_3)_2]$. This is consistent with the fact that the gold center in **4** is more electron rich than in **5**, hence less electrophilic and less prone to tricoordination.[14]

The satisfactory COPASI fitting to the experimental points in Figure 2 strongly supports the proposed mechanisms and affords a value of $K_{eq} = 2.14 \times 10^2$ mol^{-1} L ($\Delta G_{eq} = -2.9$ kcal mol^{-1}) for the fast $AsPh_3$ coordination equilibrium leading to formation of **5**. Moreover, the activation energy barrier obtained independently by least-squares adjustment of the reaction without added $AsPh_3$ (pathway **A**) is virtually identical to the value obtained in the overall COPASI fitting: $\Delta G_A^{\ddagger} = 19.2$ kcal mol^{-1}. The formation of **5**, induced by the addition of free $AsPh_3$, opens a faster transmetalation pathway **B**, with $\Delta G_B^{\ddagger} = 17.8$ kcal mol^{-1} (Scheme 1).

This work combines experimental and computational approaches to elucidate the cooperative Rf/Cl exchange pathways (**A** and **B**) using density functional theory (DFT) at the wb97xd level (see SI for details).[15,16] The kinetic experiments define the energetic profile of the process—including the relative positions of reactants and products, the rate-determining transition states, and the thermodynamics of $AsPh_3$ coordination—with high precision. In contrast, structural information on intermediates and transition states, which cannot be accessed experimentally, is provided by DFT calculations, which have been satisfactorily benchmarked against the available experimental data. To reflect this complementary use of both approaches, Figures 3 and 10 depict the Gibbs energy diagrams using a two-color scheme: black for computed values and blue for experimental data, which are used as reference due to their lower uncertainty.[17]

Computational Study of Transmetalation Pathway A. The Gibbs energy diagram of pathway **A** is shown in Figure 3. The first step involves the interaction of complexes **1** and **2** to yield a weakly interacting van der Waals complex (***I1***), which lies 3.8 kcal mol^{-1} above the energy of the separated reactants. From this intermediate, the redox-insertion of the Au center into the Rh−C bond takes place via ***TS1***, featuring a fairly symmetric Rf bridge, with a COPASI-refined activation energy of 19.2 kcal mol^{-1}.[18] This step results in formation of ***I2***, where both metal centers display square planar geometry. Using the carbene insertion processes as reaction model, the two electrons of the new Au−Rh bond in ***I2*** have been provided by gold (gold has been oxidized) while Rh has received this

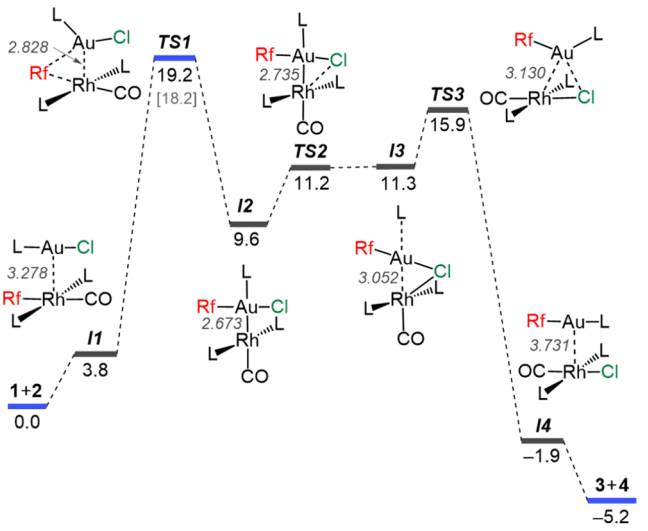

Figure 3. Gibbs energy diagram (in kcal mol^{-1}) for the transmetalation reaction between **1** and **2** in CH_2Cl_2 via pathway **A**. Rh−Au distances (Å) are also given. Blue lines highlight COPASI-refined values obtained from the experimental data. The DFT-calculated energy for ***TS1*** is shown in brackets for comparison.

donation and consequently has been reduced. This finding confirms the suspected mechanistic switch from Rh^I redox-insertion, found in our previous study,[8] to Au^I redox-insertion here. Considering that the electronegativity differences in M−M′ bonds are small, the accepted rules to assign formal metal-oxidation numbers state that M−M′ bonds do not count (as applied in metals themselves, where the structures have many M−M bonds but the formal oxidation state is assigned M^0). Consequently, we should consider ***I2*** closer to a Au^{II}−Rh^0 bimetallic molecule than to a Au^{III}−Rh^{-I} bonded species,[9] suggesting a milder oxidation (e.g., 1e donation) of the initial Au^I compound (**2**) and milder reduction (e.g., 1e acceptance) of the Rh^I reagent (**1**).[19]

Detailed analysis of the optimized structures of ***TS1*** and ***I2*** (Figure 4) shows that, while the Rf group acts as a bridging group between both metals in ***TS1*** (with typical M−C_{ipso} distances of *ca.* 2.3 Å), the Cl^- ligand remains coordinated to gold and behaves as a mere spectator. Hence, the formation of

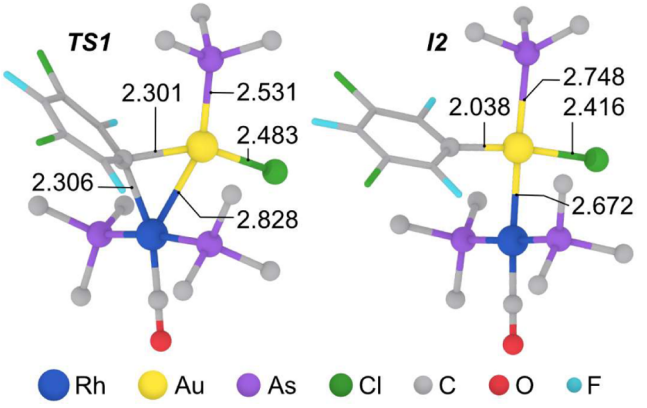

Figure 4. Ball and stick representation of the optimized structures of ***TS1*** (left) and ***I2*** (right) with selected bond distances (in Å). Ph groups in the $AsPh_3$ ligands are omitted for clarity. **Sum of covalent radii (in Å)**: Au−Rh = 2.78; Au−C = 2.09; Rh−C = 2.15; Au−As = 2.55; Au−Cl = 2.38.[20]

https://doi.org/10.1021/acs.inorgchem.5c01081
Inorg. Chem. 2025, 64, 13729−13739

a Rf bridge and a strong Au−Rh interaction (2.828 Å in ***TS1***) is preferred over transmetalation via potential Rf/Cl mixed double bridges, which would presumably involve weaker M−M′ interactions. Indeed, all our attempts to find such a double-bridged transition state with a feasible activation energy were unsuccessful. Consistently, the Au−Rh bond distance in intermediate ***I2*** (2.673 Å), somewhat shorter than the sum of covalent radii (2.78 Å),[20] is comparable to those found in single-crystal X-ray diffraction structures of related complexes (2.531 and 2.690 Å).[21] Interestingly, the remarkably long Au−As bond observed in ***I2*** is indicative of a large *trans influence* of the Au−Rh bond.[22]

In the next steps, transmetalation of the Cl group occurs in a process involving two transition states (***TS2*** and ***TS3***) of relatively low energy. In particular, ***TS2*** features an incipient very asymmetric Au−Cl−Rh bridge with a long Rh−Cl distance, and a relative energy barrier from ***I2*** of 1.6 kcal mol^{-1}. In contrast, intermediate ***I3*** displays a fairly symmetric Au−Cl−Rh bridge with Au−Cl and Rh−Cl distances moderately longer than the sum of covalent radii. The Cl transfer from Au in ***I3*** to Rh in ***I4*** is completed via ***TS3***. In this transfer the gold atom recovers the electron density involved in the Au−Rh bond, generating the van der Waals complex ***I4*** with the reaction products weakly interacting.

Does Rh(I) Oxidize Au(I)? The results of our previous study on the aryl exchange between [Au(Pf)($AsPh_3$)] (Pf = C_6F_5) and *trans*-[Rh(Rf)(CO)($AsPh_3$)$_2$] (Rf = $C_6F_3Cl_2$-3,5) (**1**) had shown that the process started with an oxidative insertion of the rhodium(I) center into the Au−C_6F_5 bond, which, as discussed, led to the formation of the Rh(II)−Au(0) intermediate [($AsPh_3$)$_2$(CO)(Rf)(Pf)Rh−Au($AsPh_3$)] (***I2***^) (Figure 5, left).[8] Herein, we have found that the Rf/Cl exchange reaction between *trans*-[Rh(Rf)(CO)($AsPh_3$)$_2$] (**1**) and [AuCl($AsPh_3$)] (**2**) is triggered by an oxidative insertion of the Au(I) center into the Rh−Rf bond, which corresponds electronically to a less expected oxidation of the Au^I center by Rh^I, yielding the Rh(0)−Au(II) intermediate [($AsPh_3$)$_2$(CO)-Rh−Au(Rf)(Cl)($AsPh_3$)] (***I2***) (Figure 5, right).

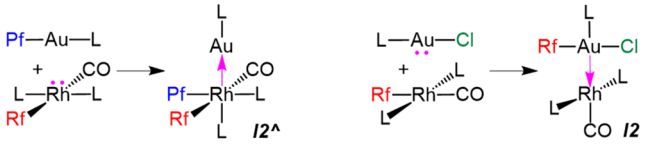

Figure 5. Reagents vs key intermediates for reactions in eqs 1 (left) and 2 (right). The donor electron pair and the dative covalent M→M′ bond formed in each case are highlighted in pink.

The joint analysis of the two redox-insertion mechanisms for the Rh/Au transmetalations, Rf/Cl here and Rf/Pf in our previous study, gives us the opportunity to consider chemical concepts operating in bimetallic species with M−M′ bonds. First of all, the idea behind the rule that metal−metal bonds do not count in the assignment of formal oxidation states of metal centers is that in highly polar bonds involving atoms of very different electronegativity (*e.g.* Rh−Rf or Au−Cl) the two bond electrons are assigned to the more electronegative group ([Rh$^+$]−[:Rf$^-$] or [Au$^+$]−[:Cl$^-$]) to reflect the loss of electron density. Thus, these bonds count as +1 in the formal oxidation state of the Rh or Au centers. The electronic polarization in metal−metal bonds (*e.g.* Rh−Au) is much smaller, and the bond electron pair is oversimplified by the classical rule, which considers this pair as equally shared by the two metal centers (zero polarization). Obviously, this is true only when the metal−metal bond connects two identical [M] fragments. Moreover, speaking of bond electron pairs is also an oversimplification because the orbitals involved in the M−M′ bond are neither purely metal orbitals nor fully centered at the metal and consequently, the potentially bonding orbitals are deeply influenced by the ligands. Anyhow, this extreme but useful approximation to bond polarization and electron density at the metal center allows us to assign Rh^I and Au^I oxidation states to complexes such as **1**−**5**. These traditional concepts can benefit from sophisticated theoretical approximations. In this line, some recent reports deal with Sanderson's principle[23] of "electronegativity *equalization*" during bond formation,[24,25] or with the concept of "chemical potentials equalization", leading to "electronegativity *equilibration*".[26] Here we use different computational approaches to compare the two transmetalation mechanisms found.

QTAIM (Quantum Theory of Atoms in Molecules) Study. The two exchange mechanisms discussed so far have in common the occurrence of metal redox-insertions with comparable DFT activation energies (***TS1*** = 18.2 kcal mol^{-1}; ***TS1***^ = 20.3 kcal mol^{-1}),[27] which give rise to the strikingly different Rh−Au bonded intermediates depicted in Figure 5, namely ***I2*** (Au and Rh are square planar) and ***I2***^ (octahedral Rh and linear Au) highlighting the mechanistic divergence between Rf/Cl and Rf/Pf transmetalations. Although the Au−

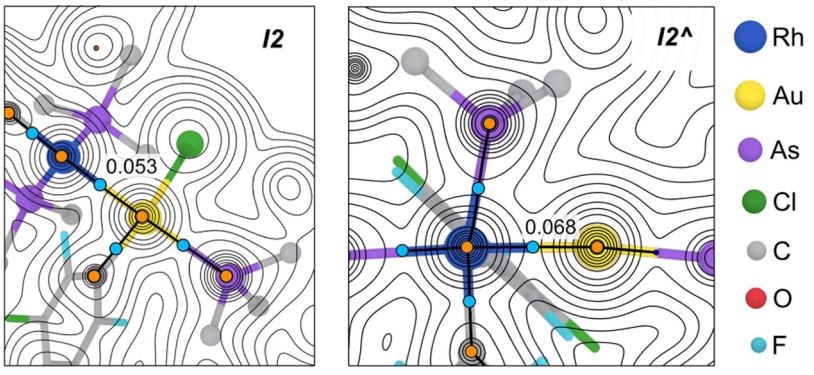

Figure 6. Topological maps obtained by QTAIM for ***I2*** (left) and ***I2***^ (right), including the electron densities (ρ(r)) found at the Rh−Au BCP. Blue and orange dots denote bond and nuclear critical points respectively. Relevant distances in Å: ***I2***: Rh−Au = 2.672; Rh−BCP = 1.231; Au−BCP = 1.441. ***I2***^: Rh−Au = 2.602; Rh−BCP = 1.316; Au−BCP = 1.286. Experimental covalent radii in Å: Rh = 1.42(7); Au = 1.36(6).[20]

https://doi.org/10.1021/acs.inorgchem.5c01081
Inorg. Chem. 2025, 64, 13729−13739

Rh bond does not count for the oxidation state number, it obviously counts for the coordination number.

Figure 6 shows the electron density maps of ***I2*** (left) and ***I2***^ (right), obtained by means of QTAIM calculations (details in SI),[28] allowing to easily identify a bond critical point (BCP 3, −1) for each Rh−Au bond. The calculated electron density at the Rh−Au BCP is lower for ***I2*** than for ***I2***^ ($\rho = 5.33 \times 10^{-2}$ and 6.85×10^{-2} respectively), as could be expected for a longer Rh−Au bond distance in ***I2*** (Rh−Au = 2.672 Å in ***I2***; Rh−Au = 2.602 Å in ***I2***^; sum of covalent radii = 2.78 Å).[20] Interestingly, the direct comparison of the M−BCP distances, and the opposite variations observed for each metal in both cases (see caption of Figure 6), further supports the changes in the Rh−Au bond polarizations exaggerated in Figure 5 as donations of an electron pair.

Extending the conventional use of sum of covalent radii to predict bond distances, we could formally consider the **Rh−BCP** and **BCP−Au** distances in each intermediate as their effective metallic radii (r_{ef}). The r_{ef} for Rh is larger in ***I2***^ (1.316 Å), where Rh is supposed to have been oxidized, polarizing some bond electron density to the domains of Au, than in ***I2*** (1.231 Å). Conversely, the r_{ef} for Au is larger in ***I2*** (1.442 Å), in which the gold center has presumably polarized some bond electron density in favor of Rh, than in ***I2***^ (1.286 Å). Thus, the r_{ef} elongation is somehow reflecting, in each case, the direction of electron polarization of the Rh−Au covalent bond pair. We propose that a larger r_{ef} reflects a higher polarization of the electron density of the corresponding metal center (equivalent to ″oxidation″) toward the counterpart in the M−M′, which undergoes ″reduction″ with concomitant shrinking of its r_{ef}. The QTAIM results support the *a priori* ″intuitive″ Rh^{I} ″oxidation″ with Rh→Au electron pair polarization in ***I2***^, and the ″counterintuitive″ Au^{I} oxidation, by Au→Rh electron pair polarization, in ***I2*** (Figure 5).

NBO (Natural Bonding Orbital) and SOPT (Second Order Perturbation Theory) Analyses. We are aware that the previous description of the M−M′ bond in ***I2*** and ***I2***^, although useful, is somehow naive since the Rh···Au interactions cannot be assigned only to a bond electron pair and the orbitals involved are not purely metal orbitals.[24] Further insight on the nature of these interactions can be obtained with NBO and SOPT analyses on the redox insertion transition states (***TS1*** and ***TS1***^) and on the key intermediates (***I2*** and ***I2***^) of both mechanisms. This allows us to identify the main donor−acceptor interactions involving participation of metal orbitals in each case (Figures 7 and 8). The ″oxidations″, ″reductions″ and bond polarizations proposed in the previous sections are well supported by the NBO results (Table 1).

The dissimilar behavior of the two gold complexes [Au(X)($AsPh_3$)] (X = C_6F_5, Cl) is related with the preferred orthogonal approximations of the linear gold molecules to the Vaska-type *trans*-[Rh(Rf)(CO)($AsPh_3$)$_2$] (**1**) square-planar complex, shown in Figures 5 and 7. In the transition state ***TS1*** the linear gold molecule [AuCl($AsPh_3$)] approaches the Rh center from above the Rf−Rh−CO axis where the Rh center is electron poorer (***TS1*** in Figure 7) and concerted slippage leads to insertion of the electron pair of the Au atom into the Rf−Rh bond. The donor orbital in ***TS1*** is the bonding orbital of the incipient Au−Rf bond, with the electron density coming mostly from C_{ipso} (88% C, 28% s and 72% p character), and only 12% from Au (95% s character). The acceptor is a hybrid Rh−CO antibonding orbital (BD*), with

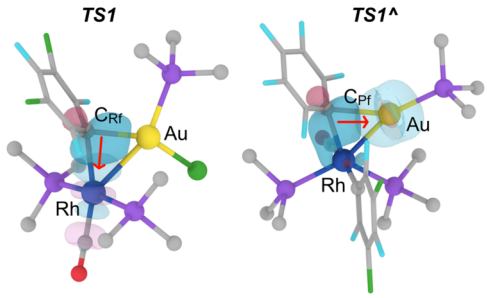

Figure 7. Simplified representation of ***TS1*** (left) and ***TS1***^ (right), with isosurfaces (isovalue = 0.07 au) of selected NBOs involved in the transmetalation. The red arrows indicate the sense of electron donation. Ph groups in the $AsPh_3$ ligands are omitted for clarity. F: light blue; Cl: green. As: violet; O: red.

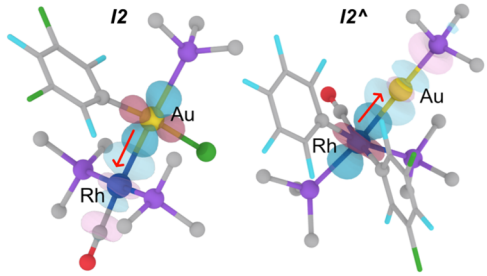

Figure 8. Isosurfaces (isovalue = 0.07 au) of selected NBOs. Left: Au^{II}→Rh^{0} intermediate (***I2***) in Rf/Cl exchange. Right: Rh^{II}→Au^{0} intermediate (***I2***^) in Rf/Pf exchange. Ph groups in the $AsPh_3$ ligands are omitted for clarity.

73% Rh contribution (46% s and 54% d character) and 27% C contribution (65% s and 35% p character). Overall, for the metals this interaction entails a partial Au oxidation by Rh with an associated SOPT energy of 100.4 kcal mol^{-1} (Table 1).

In contrast, the linear complex [Au(C_6F_5)($AsPh_3$)] approximates to the same rhodium reactant **1** over its (Ph_3As)−Rh−($AsPh_3$) axis where the Rh center is electron richer (***TS1***^ in Figure 7),[8] and concerted slippage occurs with bending of the (Ph_3As)−Rh−($AsPh_3$) angle, leading to insertion of the Rh atom into the Au−Pf bond. The donor orbital in ***TS1***^ is a bonding orbital (BD) from the incipient Rh−Pf bond, mainly centered at the C_{ipso} of the bridging aryl (83% C_{Pf}, with 28% s and 72% p character; 17% Rh, with 56% s and 44% d character). The acceptor is a low valence (LV) Au orbital constituted mostly by a gold s atomic orbital (93%). This interaction implies a partial oxidation of Rh by Au with an associated SOPT energy of 129.3 kcal mol^{-1}.

Activation strain analyses (details in SI) illustrate that the higher interaction energy between reactive fragments (E_{int}) observed for ***TS1***^ compared to ***TS1*** (71.3 vs 64.5 kcal mol^{-1}) is compensated by the also higher negative contribution of the sum of distortion energies (E_{dist}) for ***TS1***^ (see Table S5). This accounts for their similar activation barriers.

Geometry relaxations from both transition states, either evolution from ***TS1*** to ***I2*** or from ***TS1***^ to ***I2***^, complete the metal insertion processes. The dissimilar polarizations of the electron density in the Au(μ-C_{Ar})Rh bridge in each case (Figure 7), lead to formation of the Rh−Au bonds in ***I2*** or ***I2***^ with opposite donor and acceptor metal centers (Figure 8).

Figures 5 and 8 depict the main NBO interactions identified in the respective Rh−Au bonds of intermediates ***I2*** and ***I2***^. For ***I2***, we can speak of a Au^{II}→Rh^{0} donation where a filled Au

https://doi.org/10.1021/acs.inorgchem.5c01081
Inorg. Chem. 2025, 64, 13729−13739

Table 1. Selected Donor–Acceptor Interactions Identified by Means of NBO Analyses on *TS1*/*TS1*^ and on *I2*/*I2*^ Illustrated in Figures 7 and 8, Respectively[a]

species	donor	contribution	acceptor	contribution	E_{SOPT}
TS1	BD Au–C_{Rf}	88% C s (28%) p (72%) 12% Au s (95%) p (1%) d (4%)	BD* Rh–C_{CO}	73% Rh s (46%) d (54%) 27% C s (65%) p (35%)	100.4
TS1^	BD Rh–C_{Pf}	83% C s (28%) p (72%) 17% Rh s (56%) d (44%)	LV Au	Au s (93%) d (7%)	129.3
I2	LP Au	Au s (7%) d (93%)	BD* Rh–C_{CO}	73% Rh s (46%) d (54%) 27% C s (65%) p (35%)	33.8
I2^	LP Rh	Rh s (1%) d (99%)	BD* Au–As	77% Au s (92%) d (8%) 23% As s (33%) p (67%)	45.0

[a]*LP*, *LV*, *BD* and *BD** stand for Lone Pair, Low Valence, Bonding and Antibonding orbitals respectively. SOPT energies in kcal mol^{-1}.

sd orbital (93% d) acts as donor, and the acceptor is an antibonding Rh–CO orbital (73% Rh, 27% C_{CO}) mainly centered at the Rh atom (E_{SOPT} = 33.8 kcal mol^{-1}). Presumably, the CO ligand makes rhodium a better acceptor, allowing for the formal oxidation of the gold center. Conversely, a $Rh^{II}\rightarrow Au^{0}$ donation is found for ***I2***^, where the donor is an occupied lone-pair Rh orbital (99% *d character)*, and the acceptor is an antibonding Au–As orbital (77% Au, 23% As) mainly centered at the Au atom (E_{SOPT} = 45.0 kcal mol^{-1}). Notably, no interactions with comparable SOPT energies are found for donations from the corresponding reduced metals (see Table S4 for more NBO data).

In summary, NBO and SOPT analyses certainly support that the Au–Rh bond is polarized toward Rh in ***I2*** whereas the opposite holds true for ***I2***^. Consequently, Au^{I} is in fact "oxidized" by Rh^{I}, or more precisely by $Rh^{I}(CO)$, in the transmetalation reaction of *trans*-[Rh(Rf)(CO)$(AsPh_3)_2$] with [AuCl$(AsPh_3)$], whereas it is reduced by Rh^{I} in the analogous reaction with [Au$(C_6F_5)(AsPh_3)$]. However, this overall balance cannot be correctly understood if the effects of other atoms in the molecule are disregarded.

It should be noted that the analysis on which metal center undergoes the equivalent to partial oxidation or partial reduction along the mechanistic pathway (at the transition states and intermediates) should not be confused with the net result of the exchange (eqs 1 and 2) since no formal change in oxidation state occurs between reactants and products in either case.[29,30]

Electronic Structure Evidence for Rhodium Reduction in Intermediate *I2*. To further support the Rh(0)–Au(II) formulation proposed for intermediate ***I2***, a localized orbital analysis was carried out using the Pipek–Mezey method.[31] Careful examination of the molecular orbitals (MOs) of the molecule allowed the identification of the four occupied d-type valence orbitals centered on the rhodium atom. The resulting localized orbitals closely match the canonical d_{xy}, d_{xz}, d_{yz}, and d_{z^2} functions and account for 8 d-electrons (Figure 9). The topology and relative energies of the localized orbitals are also consistent with a distorted square-planar geometry, with d_{xz} and d_{yz} orbitals clearly non-degenerate due to the lack of D_{4h} symmetry.[32]

In addition, the HOMO, though not localized, unambiguously places d-type electron density on rhodium, primarily originating from gold. This orbital forms the bonding component along the Rh–Au axis and is consistent with a dative Au→Rh interaction. Conversely, the LUMO displays the corresponding Rh–Au antibonding counterpart, involving the rhodium $d_{x^2-y^2}$ atomic orbital (Figure 9). These results reinforce the formal d^9 configuration for rhodium in ***I2***,

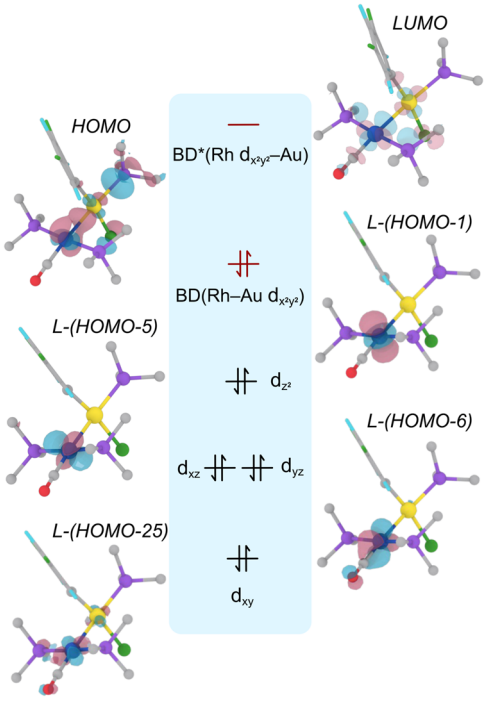

Figure 9. Pipek–Mezey localized rhodium d-orbitals (d_{xy}, d_{xz}, d_{yz}, and d_{z^2}), HOMO, and LUMO of intermediate ***I2***. Ph groups in the $AsPh_3$ ligands are omitted for clarity. Idealized orbital distribution for a D_{4h} complex with d^8 configuration is included as comparison, highlighting the inclusion of the shared Rh–Au HOMO.

implying a Rh(0) oxidation state, and more importantly, confirm the unexpected ability of gold(I) to reduce rhodium-(I).

For intermediate ***I2***^, featuring an octahedral rhodium geometry, localization of the Rh-centered d-orbitals was not feasible due to extensive mixing with ligand-based orbitals. However, the HOMO and LUMO (Figure S6) clearly show the bonding and antibonding components along the Rh–Au axis, respectively, allowing identification of the rhodium d_{z^2} orbital as the main contributor to the dative Rh→Au interaction. Although the unoccupied Rh $d_{x^2-y^2}$ orbital could not be directly localized, its contributions are evident in LUMO+3 and LUMO+5. These findings further support the formal oxidation of rhodium in ***I2***^, consistent with a rhodium(II) oxidation state.

Computational Study of the Transmetalation Pathway B. The $AsPh_3$-catalyzed character of the transmetalation pathway **B** suggests $AsPh_3$ coordination to gold (Scheme 1) and, in fact, it involves exchange between 3-coordinate

https://doi.org/10.1021/acs.inorgchem.5c01081
Inorg. Chem. 2025, 64, 13729–13739

[AuCl(AsPh$_3$)$_2$] (**5**) and *trans*-[Rh(Rf)(CO)(AsPh$_3$)$_2$] (**1**). As commented before, mass spectra confirm the formation of **5** upon AsPh$_3$ addition to [AuCl(AsPh$_3$)] (**2**) in CH_2Cl_2, and discard significant formation of [AuCl(AsPh$_3$)$_3$] in the experimental conditions. The proposed Gibbs energy diagram for pathway **B** is depicted in Figure 10 and shows that the

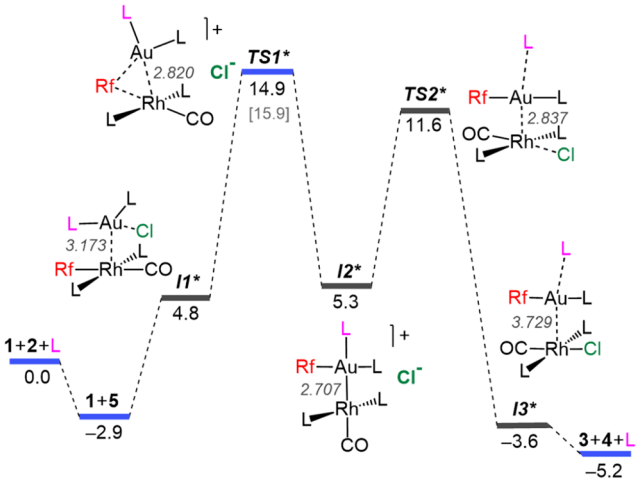

Figure 10. Gibbs energy diagram (in kcal mol^{-1}) for the ligand-promoted transmetalation between **1** and **5** (Pathway **B**) in CH_2Cl_2. Rh−Au distances (in Å) are also given. Blue lines denote COPASI-refined values obtained from experimental data. The energy of ***I2**** was referenced to the cationic ***TS1****. The DFT-calculated energy for ***TS1**** is shown in brackets for comparison (note that the overall barrier should be evaluated from the lowest energy point).

coordination of AsPh$_3$ induces the formation of ionic transition states and intermediates with dissociated Cl$^-$. Obviously, the thermodynamic balance of the catalyzed reaction is identical to the uncatalyzed one (ΔG_0 = −5.2 kcal mol^{-1}).

The equilibrium constant for the formation of **1** + **5** obtained from the microkinetic simulation corresponds to a stabilization of ΔG_{eq} = −2.9 kcal mol^{-1} associated with gold tricoordination. The van der Waals intermediate ***I1**** (added AsPh$_3$ molecule highlighted in pink) shows already a substantially elongated Au−Cl bond while both AsPh$_3$ ligands remain tightly coordinated to the gold center. Subsequently, the rate determining redox insertion occurs as in the uncatalyzed case. The tricoordination of gold in **5**, increasing its electron density compared to the linear [AuCl(AsPh$_3$)] (**2**), seems to facilitate notably this step, lowering the overall activation barrier to 17.8 kcal mol^{-1} for pathway **B**, compared to the $\Delta G^{\ddagger}$ for pathway **A** (19.2 kcal mol^{-1}, Figure 3). In contrast with the otherwise analogous ***TS1***, the Au(μ-Rf)Rh transition state ***TS1**** (Rh−Au = 2.820 Å), features a dissociated Cl$^-$ ligand, displaced from the Au coordination sphere by the additional AsPh$_3$ ligand, forming an ion-pair. Similarly to Pathway A, the hypothetical concerted mechanism involving a Au(μ-Rf)(μ-Cl)Rh transition state was computationally discarded.

Relaxation from ***TS1**** leads to ***I2****, which also displays an ion-pair nature. Structurally, the cation of ***I2**** features the expected elongation of the Au−As bond trans to Rh, and the Au−Rh distance (2.707 Å) supports a covalent bond similar to the one in ***I2***. From ***I2****, Cl$^-$ coordination to Rh induces, via ***TS2****, extrusion of the [AuRfL] (**4**) gold moiety from the Rh coordination sphere leading to ***I3**** with concomitant dissociation of the L ligand confirming the catalytic role of arsine.

The participation of ionic species along a reaction mechanism often compromises the accuracy of computational results, benchmarked against the experimental values, due to non-negligible DFT errors intimately related with poor description of solvation effects using implicit solvent models.[33] It is well-known that ionic molecules show only low conductivities in CH_2Cl_2, so it is reasonable to propose the formation of ion pairs upon AsPh$_3$ addition, instead of separated ions. Contacted ion-pair structures, as proposed for ***TS1**** and ***I2**** in Figure 10, are expected for the AsPh$_3$-promoted mechanism in CH_2Cl_2 because of its weak ion solvating strength. In favor of this proposal, when the reaction is carried out in acetone-d$_6$ (a much better ion-solvating agent than CH_2Cl_2), the accelerating effect of added AsPh$_3$ becomes remarkably higher.

The influence of the solvent on the efficiency of AsPh$_3$ as a transmetalation catalyst is noteworthy. Specifically, while the addition of 10 mol % of free ligand increases the reaction rate by 60% in CD_2Cl_2 (red vs deep blue traces in Figure 2), the same AsPh$_3$ loading in acetone-d$_6$ results in a 3.1-fold acceleration compared to the uncatalyzed system (Figure S4), making the catalytic effect approximately five times greater. Unfortunately, a full kinetic analysis in this solvent was not feasible due to limited product solubility and extremely fast reaction rates at higher AsPh$_3$ loadings. Nevertheless, these observations provide strong experimental support for the involvement of charged species in the catalyzed transmetalation mechanism. We hypothesize that the superior ability of acetone to solvate fully separated ions—unlike the more likely ion-pairing scenario in CD_2Cl_2—leads to a larger activation energy gap between the neutral (A) and ionic (B) pathways, resulting in a more pronounced catalytic effect.

The intimate details of ion-pair species in CD_2Cl_2 solutions are very complicated.[34] Fortunately, the simple ion-pair species ***TS1**** and ***I2**** dealt with in the calculations seem to represent reasonably well the system in CH_2Cl_2 solution, since the computed activation energy from **1** + **5** (18.8 kcal mol^{-1}) is remarkably close to the experimental COPASI-fitted value (17.8 kcal mol^{-1}). In addition, the structures of the isolated cations of ***TS1**** and ***I2**** were optimized (details in SI) and were found to show only negligible differences with the cationic fragments of their respective ion pairs species confirming that, in the rate limiting aryl transfer, the chloride plays a spectator role in the structural rearrangement at the cation. Finally, it is worth mentioning that both pathways, either the uncatalyzed (**A**) or the AsPh$_3$-catalyzed (**B**), unveiled for the Rf/Cl exchange (Scheme 1), have in common the formal oxidation of the gold center in the redox insertion step, as supported by the Au→Rh interactions found by the NBO studies on ***TS1**** and ***I2**** (see Figure S7).

CONCLUSIONS

The joint analysis of the Rh^I−Rf/Au^I−Cl (Rf = $C_6F_3Cl_2$-3,5) and Rh^I−Rf/Au^I−Pf (Pf = C_6F_5) transmetalation reactions reported here and in our previous paper,[8] shows that they do not follow the prototypical mechanism involving transition states with mixed double bridges, but via redox-insertion of Au into the Rh−C$_{Rf}$ bond, or of Rh into the Au−C$_{Pf}$ bond, respectively. The preferred orthogonal approximation of X−Au−L (L = AsPh$_3$) to the square planar *trans*-[RhRf(CO)L$_2$] (**1**) (Cl−Au−L lying on the Rf−Rh−CO axis, or Pf−Au−L

https://doi.org/10.1021/acs.inorgchem.5c01081
Inorg. Chem. 2025, 64, 13729−13739

lying on the L−Rh−L axis) determines the redox insertion operating (Figure 5). This study should be taken as a warning to prevent careless mechanistic misinterpretations when combining two transition metal (or group 11) complexes and might find further application in the bimetallic catalysis field.

The reaction intermediates formed upon redox insertion contain Rh−Au bonds at distances shorter than the sum of the covalent radii. In the Rf/Pf exchange, ***I2***^ featuring an octahedral Rh and linear Au was found, and further mechanistic evolution requires Rh−$AsPh_3$ dissociation previous to the rate-determining isomerization step, explaining the decelerating effect upon arsine addition reported in ref 8. In contrast, the Rf/Cl exchange implies Au insertion into the Rh−C_{Rf} bond yielding intermediates (***I2*** and ***I2****) with square planar geometries for both metal centers. This process can proceed from [$AuCl(AsPh_3)$] or, more rapidly upon $AsPh_3$ addition, from [$AuCl(AsPh_3)_2$], highlighting the catalytic role of $AsPh_3$ in the transmetalation.

Based on oxidation state assignment rules and corroborated by orbital localization studies, the formation of dative Rh−Au bonds reflects a one-electron redox process. In the Rf/Cl transmetalation, ***I2*** corresponds to a Rh(0)−Au(II) formulation, indicating that Au^{I} is oxidized by Rh^{I}(CO). Conversely, in the Rf/Pf exchange, the opposite electron flow gives rise to ***I2***^, best described as Rh(II)−Au(0). This dual behavior is further supported by NBO and SOPT analyses, which show that the oxidized metal center acts as the electron donor in each case.

Finally, we wish to emphasize the distinctive role of $AsPh_3$ as a ligand, whose moderate coordinating ability makes its binding reversible under reaction conditions—unlike stronger ligands such as PPh_3. This reversibility is key to understanding the observed kinetic effects: coordination to Au^{I} in the Rf/Cl system accelerates transmetalation, while dissociation from Rh in the Rf/Pf system (ref 8) has the opposite effect. Beyond the present study, related investigations in our group have shown that the partial dissociation of substoichiometric $AsPh_3$ plays a critical role in (a) preventing Au^{I} disproportionation of [Au(carbene)(solv)]$^+$ active species under catalytic conditions;[35] (b) enabling the Au-*co*-catalyzed Stille coupling of sterically demanding aryls;[4c] and, more recently, (c) suppressing undesired side reactivity in fluorinated aryl−alkynyl Stille couplings.[22] Although phosphines were historically essential to stabilizing organometallic species, their widespread use may have led to the underappreciation of ligands with more labile coordination. As is the case for hemilabile versus rigid chelates, monodentate arsines represent a promising and underexplored alternative when reversible binding may be mechanistically relevant.

EXPERIMENTAL SECTION

General Considerations. All reactions were performed under N_2 atmosphere. Solvents were purified according to standard procedures. Complexes *trans*-[$RhRf(CO)(AsPh_3)_2$] (**1**),[8] [$AuCl(AsPh_3)$] (**2**),[36] *trans*-[$RhCl(CO)(AsPh_3)_2$] (**3**),[37] and [$AuRf(AsPh_3)$] (**4**),[4b] were prepared following literature procedures. $AsPh_3$ and 1,3,5-trichloro-2,4,6-trifluorobenzene ($C_6F_3Cl_3$) are commercially available and were recrystallized prior to use in the kinetic experiments. Technical measurements were performed with equipment of the LTI services or the IU CINQUIMA (both University of Valladolid) unless otherwise stated.

The NMR spectra were recorded on an Agilent 500 MHz instrument. ^{1}H NMR and ^{19}F NMR spectra were referenced to TMS and $CFCl_3$, respectively. Mass spectra were obtained using a Bruker Maxis Impact time-of-flight mass spectrometer coupled with a matrix-assisted laser desorption/ionization (MALDI−TOF) Bruker Autoflex instrument. The elemental analyses were performed with a Carlo Erba 1108 microanalyser (Vigo University, Spain).

Single-crystal X-ray diffraction data were collected in an Agilent Supernova diffractometer with an Atlas CCD area detector. Data collection was performed with Mo−Kα radiation (λ = 0.71073 Å). Data integration, scaling and empirical absorption correction was performed using the CrysAlisPro program package.[38] The structure was solved with ShelxT,[39] and refined with ShelxL,[40] within the Olex2 software.[41]

No uncommon hazards are noted.

Characterization of the Fluorinated Complexes. *trans-[RhRf(CO)(AsPh$_3$)$_2$] (**1**).* NMR data (CD_2Cl_2, 293 K): ^{19}F δ − 86.25 (d, $^3J_{Fo\text{-}Rh}$ = 9.5 Hz, $2F_o$), − 122.11 (s, $1F_p$). ^{1}H δ 7.54 (m, $AsPh_3$, 12H), 7.45−7.30 (m, $AsPh_3$, 18H). Anal. Calcd for $C_{43}H_{30}As_2Cl_2F_3ORh$: C, 54.75; H, 3.21. Found: C, 54.96; H, 3.03.

*[AuRf(AsPh$_3$)$_2$] (**4**).* NMR data (CD_2Cl_2, 293 K): ^{19}F δ − 90.20 (s, $2F_o$), − 116.92 (s, $1F_p$). ^{1}H δ 7.65−7.50 (m, $AsPh_3$, 15H). Anal. Calcd for $C_{24}H_{15}AsAuCl_2F_3$: C, 41.00; H, 2.15. Found: C, 40.90; H, 2.03.

Kinetic Studies. Kinetic experiments were monitored by ^{19}F NMR. NMR tubes were charged with **1** (4.71 mg, 5.00×10^{-3} mmol), **2** (2.69 mg, 5.00×10^{-3} mmol) and $C_6F_3Cl_3$ (0.78 mg, 3.32×10^{-3} mmol) as the internal reference. Subsequently, previously cooled CD_2Cl_2 (0.50 mL), containing the appropriate amount of dissolved $AsPh_3$ depending on the experiment, was added and the tube was then placed into a thermostated probe in the NMR spectrometer. The temperature of the sample (273 K) was confirmed using methanol as a chemical shift thermometer.[42] Five minutes were allowed for temperature equilibration. Then, concentration−time data were obtained from the integrals of the F_{ortho} signals of **1** and **4**.

The experimental data collected from the individual reactions with varying concentrations of $AsPh_3$, were simultaneously fitted to the kinetic model shown in Scheme 1 by nonlinear least-squares (NLLS) regression, using the COPASI software.[12]

Computational Methods. DFT calculations reported in this work were carried out using the dispersion-corrected hybrid functional ωB97X-D,[43] implemented in the Gaussian09 software.[44] To describe the C, As, and H atoms, the double-ζ basis set 6−31G(d,p) was employed, whereas the same basis set with added diffuse functions was used for the more electronegative O, Cl, and F atoms. The Rh and Au metal centers were described using the effective core potential LANL2DZ,[45] including an *f*-polarization function (exponents: 1.350 for Rh and 1.050 for Au).[46] Geometry optimizations were performed in vacuum without imposing any constraints, and their nature was further assessed through vibrational frequency analysis. As expected, all the energy minima were confirmed to display only real vibrational frequencies, whereas transition states exhibited one single imaginary frequency. For the latter, geometry relaxations along the reaction coordinate were also carried out to confirm that they connect the corresponding reaction energy minima. Solvent effects were accounted for via single-point calculations at the vacuum-optimized geometries using the SMD solvation model and the solvent employed in experiments, *i.e.* CH_2Cl_2 (ε = 8.93).[33]

Selected bonding interactions were investigated by means of NBO and SOPT analyses.[47] The topology of the electron density was analyzed by means of QTAIM,[28] as implemented in the Multiwfn package (version 3.7),[48] using the inherited wave function from the geometry optimizations. The relevant molecular orbitals were localized using the Pipek−Mezey method,[3131] as implemented in the MOKIT Python package.[49]

ASSOCIATED CONTENT

Data Availability Statement

Additionally, all the DFT-optimized structures reported in this work are openly accessible from the ioChem-BD repository at the following link: https://iochem-bd.bsc.es/browse/handle/100/342841.

https://doi.org/10.1021/acs.inorgchem.5c01081
Inorg. Chem. 2025, 64, 13729−13739

Supporting Information

The Supporting Information is available free of charge at https://pubs.acs.org/doi/10.1021/acs.inorgchem.5c01081.

NMR spectra, kinetic details (experiments and simulations), computational specifics, and crystallographic information (PDF)

Accession Codes

Deposition Numbers 2045995 and 2108472 contain the supplementary crystallographic data for this paper. These data can be obtained free of charge via the joint Cambridge Crystallographic Data Centre (CCDC) and Fachinformationszentrum Karlsruhe Access Structures service.

AUTHOR INFORMATION

Corresponding Authors

Marconi N. Peñas-Defrutos − *IU CINQUIMA/Química Inorgánica, Facultad de Ciencias, Universidad de Valladolid, 47071 Valladolid, Spain;* orcid.org/0000-0003-4804-8751; Email: marconi_44@hotmail.com

Pablo Espinet − *IU CINQUIMA/Química Inorgánica, Facultad de Ciencias, Universidad de Valladolid, 47071 Valladolid, Spain;* orcid.org/0000-0001-8649-239X; Email: espinet@qi.uva.es

Authors

Camino Bartolomé − *IU CINQUIMA/Química Inorgánica, Facultad de Ciencias, Universidad de Valladolid, 47071 Valladolid, Spain;* orcid.org/0000-0002-8492-6825

Max García-Melchor − *School of Chemistry, CRANN and AMBER Research Centres, Trinity College Dublin, D02 PN40 Dublin 2, Ireland; Center for Cooperative Research on Alternative Energy (CIC EnergiGUNE), Basque Research and Technology Alliance (BRTA), 01510 Vitoria-Gasteiz, Spain; IKERBASQUE, Basque Foundation for Science, 48009 Bilbao, Spain;* orcid.org/0000-0003-1348-4692

Complete contact information is available at: https://pubs.acs.org/10.1021/acs.inorgchem.5c01081

Author Contributions

The manuscript was written through contributions of all authors. C.B. supervised and contributed to the experimental work (synthesis, characterization and kinetic studies). M.G.-M. computed the Gibbs energy diagrams. M.N.P.-D. carried out the kinetic analysis (experiments and simulations), the different interaction analyses, and drafted the SI. P.E. led the work and wrote the final manuscript. All authors have given approval to the final version of the manuscript.

Notes

The authors declare no competing financial interest.

ACKNOWLEDGMENTS

We thank the Spanish MINECO (Project PID2020-118547GB-I00), the University of Valladolid (CONVREC-2021-221, M.N.P.-D.) and the JCyL (Project VA016G24) for the funding provided. We also acknowledge the DJEI/DES/SFI/HEA Irish Centre for High-End Computing (ICHEC) for the provision of computational resources and Manting Mu for her valuable contribution to the figure design. On the occasion of his 70th birthday, this work is dedicated to Prof. Agustí Lledós (Universitat Autònoma de Barcelona) in recognition of his outstanding contribution to establishing computational chemistry as a strong and fertile research field in Spain.

REFERENCES

(1) Carrasco, D.; García-Melchor, M.; Casares, J. A.; Espinet, P. Dramatic mechanistic switch in Sn/Au^{I} group exchanges: transmetalation vs. oxidative addition. *Chem. Commun.* **2016**, *52*, 4305−4308.

(2) (a) Pérez-Temprano, M. H.; Casares, J. A.; Espinet, P. Bimetallic Catalysis Using Transition and Group 11 Metals: An Emerging Tool for C−C Coupling and Other Reactions. *Chem. - Eur. J.* **2012**, *18*, 1864−1884. (b) Pye, D. R.; Mankad, N. P. Bimetallic catalysis for C−C and C−X coupling reactions. *Chem. Sci.* **2017**, *8*, 1705−1718.

(3) For example: (a) Oeschger, R. J.; Chen, P. Structure and Gas-Phase Thermochemistry of a Pd/Cu Complex: Studies on a Model for Transmetalation Transition States. *J. Am. Chem. Soc.* **2017**, *139*, 1069−1072. (b) Oi, M.; Takita, R.; Kanazawa, J.; Muranaka, A.; Wang, C.; Uchiyama, M. Organocopper cross-coupling reaction for C−C bond formation on highly sterically hindered structures. *Chem. Sci.* **2019**, *10*, 6107−6112.

(4) For mechanistic studies of Pd/Au transmetalations see: (a) Villar, P.; Pérez-Temprano, M. H.; Casares, J. A.; Álvarez, R.; Espinet, P. Experimental and DFT Study of the [AuAr(AsPh$_3$)]-Catalyzed cis/trans Isomerization of [PdAr$_2$(AsPh$_3$)$_2$] (Ar = C_6F_5 or $C_6Cl_2F_3$): Alternative Mechanisms and Its Switch upon Pt for Pd Substitution. *Organometallics* **2020**, *39*, 2295−2303. (b) Pérez-Temprano, M. H.; Casares, J. A.; de Lera, A. R.; Álvarez, R.; Espinet, P. Strong Metallophilic Interactions in the Palladium Arylation by Gold Aryls. *Angew. Chem., Int. Ed.* **2012**, *51*, 4917−4920. For Pd/Au catalysis see: (c) delPozo, J.; Carrasco, D.; Pérez-Temprano, M. H.; García-Melchor, M.; Álvarez, R.; Casares, J. A.; Espinet, P. Stille Coupling Involving Bulky Groups Feasible with Gold Cocatalyst. *Angew. Chem., Int. Ed.* **2013**, *52*, 2189−2193.

(5) Ponce-de-León, J.; Marcos-Ayuso, G.; Casares, J. A.; Espinet, P. Pd/Cu bimetallic catalysis to access highly fluorinated biaryls from aryl halides and fluorinated arenes. *Chem. Commun.* **2022**, *58*, 3146−3149.

(6) Alférez, M. G.; Moreno, J. J.; Hidalgo, N.; Campos, J. Reversible Hydride Migration from C_5Me_5 to Rh^{I} Revealed by a Cooperative Bimetallic Approach. *Angew. Chem., Int. Ed.* **2020**, *59*, 20863−20867.

(7) For Au^{I}-to-Rh^{III} transmetalations see: (a) Shi, Y.; Blum, S. A. Gold and Rhodium Transmetalation: Mechanistic Insights and Dual-Metal Reactivity. *Organometallics* **2011**, *30*, 1776−1779. For a recent example of Rh^{III}-to-Au^{III} transmetalation see: (b) Martín, J.; Gómez-Bengoa, E.; Genoux, A.; Nevado, C. Synthesis of Cyclometalated Gold(III) Complexes via Catalytic Rhodium to Gold(III) Transmetalation. *Angew. Chem., Int. Ed.* **2022**, *61*, No. e202116755.

(8) Peñas-Defrutos, M. N.; Bartolomé, C.; García-Melchor, M.; Espinet, P. Rh^{I}Ar/Au^{I}Ar′ Transmetalation: A Case of Group Exchange Pivoting on the Formation of M−M′ Bonds through Oxidative Insertion. *Angew. Chem., Int. Ed.* **2019**, *58*, 3501−3505.

(9) M−M′ bonds do not count for the formal oxidation number (FON), hence each metal changes only in one unit its FON. In our previous work (ref 8) we used the term "oxidative insertion" instead of "redox-insertion" but, since one metal is oxidized while the other is reduced, we believe that *redox-insertion* is more appropriate.

(10) The aryl Rf is chosen for the simplicity of its ^{19}F NMR signals, and the Rh system because of the high thermodynamic preference of the trans disposition (both for **1** and **3** complexes), which avoids the formation of other isomers. The same neutral ligand (AsPh$_3$) is used for Au and Rh compounds in order to prevent multiplication of signals due exclusively to ligand scrambling.

(11) Obviously, only **1** and **4** are observed by ^{19}F NMR (^{1}H NMR is not informative in our case). $C_6F_3Cl_3$-1,3,5 is used as internal standard.

(12) Hoops, S.; Sahle, S.; Gauges, R.; Lee, C.; Pahle, J.; Simus, N.; Singhal, M.; Xu, L.; Mendes, P.; Kummer, U. COPASI—a COmplex PAthway Simulator. *Bioinformatics* **2006**, *22*, 3067−3074.

(13) For [AuCl(AsPh$_3$)] see: (a) Weissbart, B.; Larson, L. J.; Olmstead, M. M.; Nash, C. P.; Tinti, D. S. Crystal Structures and Spectra of Two Forms of Chloro (triphenylarsine) gold(I). *Inorg. Chem.* **1995**, *34*, 393−395. For [AuX(AsPh$_3$)$_m$] (*m* = 2, 3) see:

(b) Bowmaker, G. A.; Healy, P. C.; Sobolev, A. N.; White, A. H. Synthesis and Structures of Bis- and Tris-(triphenylarsine)gold(I) Iodides. *Aust. J. Chem.* **2020**, *73*, 497−503.
(14) (a) Joost, M.; Amgoune, A.; Bourissou, D. Reactivity of Gold Complexes towards Elementary Organometallic Reactions. *Angew. Chem., Int. Ed.* **2015**, *54*, 15022−15045. (b) Joost, M.; Zeineddine, A.; Estévez, L.; Mallet-Ladeira, S.; Miqueu, K.; Amgoune, A.; Bourissou, D. Facile Oxidative Addition of Aryl Iodides to Gold(I) by Ligand Design: Bending Turns on Reactivity. *J. Am. Chem. Soc.* **2014**, *136*, 14654−14657. (c) Yang, Y.; Eberle, L.; Mulks, F. F.; Wunsch, J. F.; Zimmer, M.; Rominger, F.; Rudolph, M.; Hashmi, A. S. K. Trans Influence of Ligands on the Oxidation of Gold(I) Complexes. *J. Am. Chem. Soc.* **2019**, *141*, 17414−17420.
(15) The structures of all intermediates and TSs are available online at the following iochem-BD link: https://iochem-bd.bsc.es/browse/handle/100/342841https://iochem-bd.bsc.es/browse/handle/100/342841.
(16) Other popular functionals have been reported to overestimate the energy associated to d^8−d^{10} bonds: Oeschger, R. J.; Bissig, R.; Chen, P. Model Compounds for Intermediates and Transition States in Sonogashira and Negishi Coupling: d^8−d^{10} Bonds in Large Heterobimetallic Complexes Are Weaker than Computational Chemistry Predicts. *J. Am. Chem. Soc.* **2022**, *144*, 10330−10343.
(17) Sieffert, N.; Bühl, M. Noncovalent Interactions in a Transition-Metal Triphenylphosphine Complex: a Density Functional Case Study. *Inorg. Chem.* **2009**, *48*, 4622−4624.
(18) The computed activation energy for ***TS1*** is 18.2 kcal mol^{-1}, within 1 kcal mol^{-1} from the experimental benchmark value.
(19) This classic rule of thumb can be found in Inorganic Chemistry textbooks and helps to see at fast glance that the electronic rearrangements involving formation of M−M′ bonds can require lower polarization and lower energetic barriers.
(20) Cordero, B.; Gómez, V.; Platero-Prats, A. E.; Revés, M.; Echeverría, J.; Cremades, E.; Barragán, F.; Alvarez, S. Covalent radii revisited. *Dalton Trans.* **2008**, 2832−2838.
(21) Bianchini, C.; Elsevier, C. J.; Ernsting, J. M.; Peruzzini, M.; Zanobini, F. Control of the Bridgehead Donor Atom in the Tripodal Ligand over Oxidative Addition of $Au(PPh_3)^+$ to $[X(CH_2CH_2PPh_2)_3RhH]$ (X = N, P). X-ray Diffraction and Multinuclear (^{103}Rh, ^{31}P, ^{1}H) NMR Studies. *Inorg. Chem.* **1995**, *34*, 84−92.
(22) A similar effect was crystallographically confirmed for the Pd−Sn bond: Marcos-Ayuso, G.; Peñas-Defrutos, M. N.; Gallego, A. M.; García-Melchor, M.; Martínez-Ilarduya, J. M.; Espinet, P. Problematic Ar^F−Alkynyl Coupling with Fluorinated Aryls. From Partial Success with Alkynyl Stannanes to Efficient Solutions via Mechanistic Understanding of the Hidden Complexity. *J. Am. Chem. Soc.* **2023**, *145*, 527−536.
(23) (a) Sanderson, R. T. An Interpretation of Bond Lengths and a Classification of Bonds. *Science* **1951**, *114*, 670−672. (b) Sanderson, R. T. Electronegativity and bond energy. *J. Am. Chem. Soc.* **1983**, *105*, 2259−2261.
(24) Ferro-Costas, D.; Pérez-Juste, I.; Mosquera, R. A. Electronegativity estimator built on QTAIM-based domains of the bond electron density. *J. Comput. Chem.* **2014**, *35*, 978−985.
(25) Casals-Sainz, J. L.; Francisco, E.; Pendás, A. M. Electronegativity equalization: taming an old problem with new tools. *Phys. Chem, Chem. Phys.* **2020**, *22*, 22880−22884.
(26) Sessa, F.; Rahm, M. Electronegativity Equilibration. *J. Phys. Chem. A* **2022**, *126*, 5472−5482.
(27) The *rds* and highest activation energy in ref 8 corresponds to an isomerization process (22.3 kcal mol^{-1}), not to the redox-insertion.
(28) Bader, R. F. W. *Atoms in Molecules: A Quantum Theory*; Oxford University Press, 1990.
(29) In the Rf/Pf transmetalation (eq 1), the electronegativity of Pf and Rf is similar. Thus, their exchange does not alter significantly the stability of the system ($\Delta G_0 \approx 0$, $K_{eq} \approx 1$). In contrast, for the Rf/Cl exchange (eq 2) the equilibrium is largely shifted to the formation of the products, reaching a substantial stabilization of the system ($\Delta G_0 = -5.2$ kcal mol−1, Keq $\approx 7.0 \times 10^3$) when Cl is bonded to Rh(I).
(30) For fascinating examples of the flexibility of electron density polarization when metal atoms are involved see, for example: Duanmu, K.; Truhlar, D. G. Partial Ionic Character beyond the Pauling Paradigm: Metal Nanoparticles. *J. Phys. Chem. C* **2014**, *118*, 28069−28074.
(31) Pipek, J.; Mezey, P. G. A fast intrinsic localization procedure applicable for ab initio and semiempirical linear combination of atomic orbital wave functions. *J. Chem. Phys.* **1989**, *90*, 4916−4926.
(32) For orbital analyses based on a D_{4h} $Pd^{II}L_4$ compound (d^8 configuration) see: Börgel, J.; Campbell, M. G.; Ritter, T. Transition Metal d-Orbital Splitting Diagrams: An Updated Educational Resource for Square Planar Transition Metal Complexes. *J. Chem. Educ.* **2016**, *93*, 118−121.
(33) Marenich, A. V.; Cramer, C. J.; Truhlar, D. G. Universal Solvation Model Based on Solute Electron Density and on a Continuum Model of the Solvent Defined by the Bulk Dielectric Constant and Atomic Surface Tensions. *J. Phys. Chem. B* **2009**, *113*, 6378−6396.
(34) (a) Dukhin, A.; Parlia, S.; Somasundaran, P. Ion-Pair Conductivity Theory V: Critical Ion Size and Range of Ion-Pair Existence. *J. Electrochem. Soc.* **2018**, *165*, No. E784. (b) Iseda, K.; Kokado, K.; Sada, K. Direct Detection of the Ion Pair to Free Ions Transformation upon Complexation with an Ion Receptor in Non-Polar Solvents by using Conductometry. *ChemistryOpen* **2018**, *7*, 269−274. (c) Gestblom, B.; Songstad, J.; et al. Solvent Properties of Dichloromethane. VI. Dielectric Properties of Electrolytes in Dichloromethane. *Acta Chem. Scand.* **1987**, *41B*, 396−409.
(35) Bartolomé, C.; Ramiro, Z.; Peñas-Defrutos, M. N.; Espinet, P. Some Singular Features of Gold Catalysis: Protection of Gold(I) Catalysts by Substoichiometric Agents and Associated Phenomena. *ACS Catal.* **2016**, *6*, 6537−6545.
(36) Nieto-Oberhuber, C.; López, S.; Echavarren, A. M. Intramolecular [4 + 2] Cycloadditions of 1,3-Enynes or Arylalkynes with Alkenes with Highly Reactive Cationic Phosphine Au(I) Complexes. *J. Am. Chem. Soc.* **2005**, *127*, 6178−6179.
(37) Osborn, J. A.; Wilkinson, G.; Evans, D.; et al. *Trans*-Chlorocarbonylbis(Tri-Phenylphosphine)Rhodium and Related Complexes. *Inorg. Synth.* **1968**, *11*, 99−101.
(38) *CrysAlisPro Software system, version 1.171.33.51*; Oxford Diffraction Ltd: Oxford, UK, 2009.
(39) Sheldrick, G. M. SHELXT − Integrated space-group and crystal-structure determination. *Acta Crystallogr.* **2015**, *A71*, 3−8.
(40) Sheldrick, G. M. Crystal structure refinement with SHELXL. *Acta Cryst.* **2015**, *C71*, 3−8.
(41) Dolomanov, O. V.; Bourhis, L. J.; Gildea, R. J.; Howard, J. A. K.; Puschmann, H. OLEX2: a complete structure solution, refinement and analysis program. *J. Appl. Crystallogr.* **2009**, *42*, 339−341.
(42) Ammann, C.; Meier, P.; Merbach, A. E. A Simple Multinuclear NMR Thermometer. *J. Magn. Reson.* **1982**, *46*, 319−321.
(43) Chai, J.-D.; Head-Gordon, M. Systematic optimization of long-range corrected hybrid density functionals. *Phys. Chem. Chem. Phys.* **2008**, *10*, 6615−6620.
(44) Frisch, M. J.; Trucks, G. W.; Schlegel, H. B.; Scuseria, G. E.; Robb, M. A.; Cheeseman, J. R.; Scalmani, G.; Barone, V.; Mennucci, B.; Petersson, G. A.; Nakatsuji, H.; Caricato, M.; Li, X.; Hratchian, H. P.; Izmaylov, A. F.; Bloino, J.; Zheng, G.; Sonnenberg, J. L.; Hada, M.; Ehara, M.; Toyota, K.; Fukuda, R.; Hasegawa, J.; Ishida, M.; Nakajima, T.; Honda, Y.; Kitao, O.; Nakai, H.; Vreven, T.; Montgomery, J. A., Jr.; Peralta, J. E.; Ogliaro, F.; Bearpark, M.; Heyd, J. J.; Brothers, E.; Kudin, K. N.; Staroverov, V. N.; Kobayashi, R.; Normand, J.; Raghavachari, K.; Rendell, A.; Burant, J. C.; Iyengar, S. S.; Tomasi, J.; Cossi, M.; Rega, N.; Millam, J. M.; Klene, M.; Knox, J. E.; Cross, J. B.; Bakken, V.; Adamo, C.; Jaramillo, J.; Gomperts, R.; Stratmann, R. E.; Yazyev, O.; Austin, A. J.; Cammi, R.; Pomelli, C.; Ochterski, J. W.; Martin, R. L.; Morokuma, K.; Zakrzewski, V. G.; Voth, G. A.; Salvador, P.; Dannenberg, J. J.; Dapprich, S.; Daniels, A. D.; Farkas, Ö.; Foresman, J. B. *Gaussian 09*, Revision E.01; Gaussian, Inc.: Wallingford CT, 2009.

https://doi.org/10.1021/acs.inorgchem.5c01081
Inorg. Chem. 2025, 64, 13729−13739

(45) (a) Hay, P. J.; Wadt, W. R. Ab initio effective core potentials for molecular calculations. Potentials for the transition metal atoms Sc to Hg. *J. Chem. Phys.* **1985**, *82*, 270−283. (b) Hay, P. J.; Wadt, W. R. Ab initio effective core potentials for molecular calculations. Potentials for K to Au including the outermost core orbitals. *J. Chem. Phys.* **1985**, *82*, 299−310.
(46) Ehlers, A. W.; Biihme, M.; Dapprich, S.; Gobbi, A.; Hijllwarth, A.; Jonas, V.; Kiihler, K. F.; Stegmann, R.; Veldkamp, A.; Frenking, G. A set of f-polarization functions for pseudo-potential basis sets of the transition metals Sc-Cu, Y-Ag and La-Au. *Chem. Phys. Lett.* **1993**, *208*, 111−114.
(47) Glendening, E. D.; Badenhoop, J. K.; Reed, A. E.; Carpenter, J. E.; Bohmann, J. A.; Morales, C. M.; Landis, C. R.; Weinhold, F. *NBO 6.0*; Theoretical Chemistry Institute, University of Wisconsin: Madison, WI, 2013, http://nbo6.chem.wisc.edu/.
(48) Lu, T.; Chen, F. J. Multiwfn: A multifunctional wavefunction analyzer. *Comput. Chem.* **2012**, *33*, 580−592.
(49) Zou, J. MOKIT Program. hpps://gitlab.com/jxzou/mokit (accessed April 13, 2024).

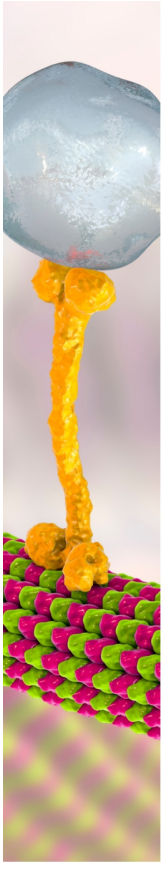
CAS BIOFINDER DISCOVERY PLATFORM™
BRIDGE BIOLOGY AND CHEMISTRY FOR FASTER ANSWERS
Analyze target relationships, compound effects, and disease pathways
Explore the platform
CAS
A division of the American Chemical Society

https://doi.org/10.1021/acs.inorgchem.5c01081
Inorg. Chem. 2025, 64, 13729−13739